Monthly Notices
of the
ROYAL ASTRONOMICAL SOCIETY

MNRAS **435,** 2896–2902 (2013)
Advance Access publication 2013 September 23

doi:10.1093/mnras/stt1484

Towards a dynamical mass of the ultraluminous X-ray source NGC 5408 X-1

D. Cseh,[1,2]⋆ F. Grisé,[3,4,5] P. Kaaret,[5] S. Corbel,[2] S. Scaringi,[1,6] P. Groot,[1] H. Falcke[1,7,8] and E. Körding[1]

[1]*Department of Astrophysics/IMAPP, Radboud University Nijmegen, PO Box 9010, NL-6500 GL Nijmegen, the Netherlands*
[2]*Laboratoire Astrophysique des Interactions Multi-echelles (UMR 7158), CEA/DSM-CNRS-Universite Paris Diderot, CEA Saclay, F-91191 Gif sur Yvette, France*
[3]*Instituto de Astrofísica de Canarias, E-38200 La Laguna, Tenerife, Spain*
[4]*Departamento de Astrofísica, Universidad de La Laguna, Avda. Astrofísico Francisco Sanchez s/n, E-38271 La Laguna, Tenerife, Spain*
[5]*Department of Physics and Astronomy, Iowa City, 52240, USA*
[6]*Instituut voor Sterrenkunde, KU Leuven, Celestijnenlaan 200D, B-3001 Leuven, Belgium*
[7]*ASTRON, NL-7990 AA Dwingeloo, the Netherlands*
[8]*Max-Planck-Institut für Radioastronomie, D-53121 Bonn, Germany*

Accepted 2013 August 5. Received 2013 July 30; in original form 2013 June 17

ABSTRACT

We obtained multi-epoch Very Large Telescope optical spectroscopic data in 2011 and 2012 on the ultraluminous X-ray source NGC 5408 X-1. We confirm that the He II λ4686 line has a broad component with an average full width at half-maximum of $v = 780 \pm 64\,\mathrm{km\,s^{-1}}$ with a variation of ∼13 per cent during observations spanning over four years, and is consistent with the origin in the accretion disc. The deepest optical spectrum does not reveal any absorption line from a donor star. Our aim was to measure the radial velocity curve and estimate the parameters of the binary system. We find an upper limit on the semi-amplitude of the radial velocity of $K = 132 \pm 42\,\mathrm{km\,s^{-1}}$. A search for a periodic signal in the data resulted in no statistically significant period. The mass function and constraints on the binary system imply a black hole mass of less than ∼510 $\mathrm{M_\odot}$. Whilst, a disc irradiation model may imply a black hole mass smaller than ∼431–1985 $\mathrm{M_\odot}$, depending on inclination. Our data can also be consistent with an unexplored orbital period range from a couple of hours to a few days, thus with a stellar-mass black hole and a subgiant companion.

Key words: accretion, accretion discs – black hole physics – X-rays: binaries.

1 INTRODUCTION

Ultraluminous X-ray sources (ULXs) are non-nuclear, accreting binary systems in external galaxies with an X-ray luminosity greater than the Eddington-limit of a 20-$\mathrm{M_\odot}$ black hole ($L_\mathrm{X} > 3 \times 10^{39}\,\mathrm{erg\,s^{-1}}$), assuming isotropic emission. Several explanations exist for the ULX phenomenon: these sources could possibly be mechanically or relativistically beamed, possibly accrete above their Eddington limit, or represent the high end of the population of stellar-mass black holes with masses of 20–100 $\mathrm{M_\odot}$ (see review by Feng & Soria 2011). A class of ULXs, called hyperluminous X-ray sources, are the best candidate intermediate-mass black holes (10^2–10^5 $\mathrm{M_\odot}$) due to their high X-ray luminosities of $L_\mathrm{X} > 10^{41}\,\mathrm{erg\,s^{-1}}$ (Kaaret, Simet & Lang 2006; Farrell et al. 2009; Walton et al. 2011; Sutton et al. 2012; Webb et al. 2012).

The remedy for the degeneracies between the above mentioned theoretical models is dynamical mass measurements of the binary system. However, it is difficult to obtain any radial velocity curve due to the fact that the most nearby ULXs lie at a distance of 3–5 Mpc, which results in faint ($V \sim$ 22–24 mag) optical counterparts. Furthermore, many optical counterparts show variable emission indicative of a dominant contribution from an accretion disc rather than a donor star (Tao et al. 2011; Grisé et al. 2012; Soria et al. 2012; Gladstone et al. 2013). So far only two ULXs: P13 (Motch et al. 2011) and M101-ULX1 (Liu 2009) show absorption lines from a late type B supergiant and emission lines from a Wolf–Rayet donor, respectively. Their typical X-ray luminosity is $\sim 10^{39}\,\mathrm{erg\,s^{-1}}$.

On the other hand, one can study the periodic variation of the X-ray (e.g. Kaaret et al. 2006; Foster et al. 2013) or the optical (e.g. Zampieri et al. 2012) light curve of ULXs, or the broad permitted lines in the optical spectra. Broad permitted lines can be produced in the dense regions of the accretion disc reflecting the velocity

⋆E-mail: d.cseh@astro.ru.nl

distribution of the inner disc. The velocity shifts of such lines may trace the orbital motion of the system and provide constraints on the mass of the compact object (Hutchings et al. 1987). In principle, the He II λ4686 line is the most promising tracer due to its highest ionization potential in the optical band. However, several studies were made using this method, e.g. on Holmberg IX X-1, NGC 1313 X-2 (Roberts et al. 2011; Liu, Orosz & Bregman 2012) and NGC 5408 X-1 (Cseh et al. 2011) resulting in no firm mass constraints. This can be due to several reasons, like insufficient time sampling of the radial velocity curve, insufficient spectral resolution resulting in blurred narrow and broad components, differing viewing geometries of the system, or a non-disc origin of the He II line. We also note that in a number of low-mass X-ray binaries (LMXBs) and cataclysmic variables the radial velocity variation of disc emission lines mostly traces the orbital period, but the associated amplitude is likely to be off from the true amplitude (e.g. Groot, Rutten & van Paradijs 2001a; Cantrell & Bailyn 2007).

NGC 5408 X-1 is a bona fide ULX reaching an X-ray luminosity of $10^{40}\,\mathrm{erg\,s^{-1}}$. It is surrounded by a photoionized optical nebula (Kaaret & Corbel 2009; Cseh et al. 2012; Grisé et al. 2012) and it is one of the few ULXs associated with a radio nebula (Kaaret et al. 2003; Lang et al. 2007; Cseh et al. 2012). The energetics of the optical nebula suggests that this ULX is, at most, mildly beamed (Kaaret & Corbel 2009) leaving the possibility of a stellar-mass black hole accreting at super-Eddington rates or a sub-Eddington but more massive stellar-mass black hole.

Strohmayer (2009) reported an orbital period of ∼115 d inferred from the X-ray light curve. On the other hand, Foster, Charles & Holley-Bockelmann (2010) suggested that this period is superorbital in nature. Four years of *Swift*/XRT monitoring revealed that after a few cycles this period disappeared and therefore is unlikely to be the orbital period (Grisé et al. 2013). However, quasi-periodic dipping behaviour with a period of 250 ± 28 d was revealed (Grisé et al. 2013; Pasham & Strohmayer 2013). Pasham & Strohmayer (2013) argue that the dipping period may reflect the orbital period of the system or can occur due to a precessing accretion disc as well.

The optical counterpart of the ULX point source was identified by Lang et al. (2007) and its X-ray to NIR SED was studied by Grisé et al. (2012), who found that it can be consistent with either a disc irradiation model or a B0I supergiant. The optical spectrum of NGC 5408 X-1 shows permitted and forbidden emission lines indicative of an X-ray photoionized nebula, and no absorption lines from a donor star. A higher resolution optical spectrum revealed the presence of broad and narrow components of permitted lines indicative of a distinct origin: likely the disc and the nebula, respectively (Cseh et al. 2011). The He II line is markedly shifted between two observations and assuming that this shift traces the orbital motion of the system an upper limit on the mass of the black hole of $\sim 1800\,\mathrm{M}_\odot$ was set (Cseh et al. 2011).

Here, we present results of multi-epoch Very Large Telescope (VLT) spectroscopic observations from 2011 and 2012 that aimed to measure the radial velocity curve of NGC 5408 X-1. We describe our observations in Section 2, our results in Section 3, and discuss the binary parameters in Section 4.

2 OBSERVATIONS

We conducted multi-epoch VLT observations in order to measure the radial velocity curve of NGC 5408 X-1 (PI: Cseh). FORS-2 observations were obtained in 2011 and in 2012 using the 1200B grism with a slit width of 0.7 arcsec covering the spectral range of 3660−5110 Å with a dispersion of 0.36 Å pixel^{-1} and a spectral resolution of $\lambda/\Delta\lambda = 1420$ at the central wavelengths. Each observing block (OB) consisted of three 850 s exposures in 2011 and three 880 s exposures in 2012 with a 12 pixel offset along the spatial axis between successive exposures. We note that OBs from 2008 were taken with a lower resolution 600B grism. See Table 1 for more details. We note that OB9 was re-observed due to seeing conditions; however, the data quality was good enough to include in our analysis. On the other hand, only 11 out of 20 OBs were scheduled and observed in 2012 due to weather conditions. CCD pixels were binned by 2 in both the spatial and spectral dimensions.

Table 1. VLT FORS observations of NGC 5408 X-1.

OB	Start	Duration (s)	Seeing (arcsec)
OBa	2008-04-08 04:59:04	3 × 850	0.78
OBb	2008-04-08 05:46:04	3 × 850	0.80
OBc	2008-04-08 06:45:13	3 × 850	0.89
OBd	2008-04-09 05:46:17	3 × 850	1.14
OBe	2008-04-10 05:08:33	3 × 850	0.67
OBf	2008-04-10 05:54:29	3 × 850	0.67
OBg	2010-04-12 07:46:55	3 × 850	0.46
OB1	2011-04-03 06:31:33	3 × 850	0.66
OB2	2011-04-11 05:23:49	3 × 850	0.63
OB3	2011-04-27 05:55:08	3 × 850	0.74
OB4	2011-05-09 04:33:47	3 × 850	0.64
OB5	2011-05-23 02:27:10	3 × 850	0.98
OB6	2011-05-26 01:26:51	3 × 850	0.87
OB7	2011-06-09 05:21:40	3 × 850	0.65
OB8	2011-06-26 03:15:13	3 × 850	0.66
OB9a	2011-06-29 00:36:08	3 × 850	1.15
OB9b	2011-07-01 02:17:41	3 × 850	0.64
OB10	2011-07-02 02:07:09	1 × 418 + 3 × 850	0.63
OB11	2012-04-15 02:55:28	3 × 880	0.65
OB12	2012-04-22 05:59:24	3 × 880	0.48
OB13	2012-04-23 03:55:59	3 × 880	0.66
OB14	2012-05-18 04:03:11	3 × 880	0.70
OB15	2012-05-20 05:16:41	3 × 880	0.64
OB16	2012-06-18 01:08:53	3 × 880	0.79
OB17	2012-06-21 00:25:03	3 × 880	1.02
OB18	2012-06-23 01:26:44	3 × 880	0.74
OB19	2012-07-18 23:49:35	3 × 880	0.86
OB20	2012-08-12 23:54:35	3 × 880	1.00
OB21	2012-08-14 23:47:47	3 × 880	0.79

The start date of each OBs in UT, the duration of successive exposures and the averaged seeing corrected by airmass during each observation. OBa–OBf are adapted from Kaaret & Corbel (2009), OBg is adapted from Cseh et al. (2011).

We reduced the data using the Image Reduction and Analysis Facility (IRAF)[1] (Tody 1993). After correcting the three exposures in each OB using bias and flat-field images, we aligned and median averaged them to eliminate bad pixels and cosmic rays using the `imcombine` task with the `ccdclip` rejection algorithm.

Due to the dimness of the ULX counterpart we used a bright nearby star at 2MASS position $\alpha_{\mathrm{J2000}} = 14^{\mathrm{h}}03^{\mathrm{m}}18\overset{\mathrm{s}}{.}97$, $\delta_{\mathrm{J2000}} = -41^\circ 22' 56\overset{''}{.}6$ as a reference trace. The slit position angle

[1] IRAF is distributed by the National Optical Astronomy Observatory, which is operated by the Association of Universities for Research in Astronomy, Inc., under cooperative agreement with the National Science Foundation.

Table 2. The broad component of the He II line.

OB	MJD	Wavelength (Å)	v_s (km s^{-1})	$v_{s,err}$ (km s^{-1})	FWHM (Å)	Flux
OBc	54 564.291 740	4692.08 ± 0.77	148.5	49.3	11.09 ± 1.44	0.56 ± 0.20
OBe	54 566.224 608	4690.03 ± 1.43	16.5	91.3	11.75 ± 1.33	0.49 ± 0.13
OBf	54 566.256 508	4689.94 ± 1.70	10.8	108.8	10.82 ± 1.55	0.53 ± 0.15
OBg	55 298.334 603	4694.63 ± 0.25	310.2	16.0	12.37 ± 0.69	1.12 ± 0.08
OB2	55 662.235 202	4692.04 ± 0.26	145.1	16.6	10.51 ± 0.62	0.81 ± 0.05
OB4	55 690.200 478	4693.99 ± 0.24	257.5	15.4	13.89 ± 0.66	0.85 ± 0.04
OB5	55 704.112 531	4692.36 ± 0.26	147.1	16.6	13.01 ± 0.63	0.85 ± 0.04
OB6	55 707.070 653	4692.88 ± 0.22	179.1	14.1	11.69 ± 0.57	1.01 ± 0.05
OB8	55 738.145 904	4693.75 ± 0.11	223.7	7.0	10.42 ± 0.31	1.69 ± 0.06
OB9a	55 741.035 417	4693.02 ± 0.27	176.2	17.3	12.53 ± 0.71	0.80 ± 0.05
OB9b	55 743.105 957	4694.68 ± 0.20	281.9	12.8	12.86 ± 0.55	1.26 ± 0.06
OB10	55 744.095 981	4692.12 ± 0.27	117.8	17.3	13.64 ± 0.64	1.98 ± 0.10
OB11	56 032.132 541	4690.56 ± 0.79	48.4	50.5	14.28 ± 1.75	0.31 ± 0.04
OB12	56 039.260 256	4694.11 ± 0.46	272.4	29.4	14.19 ± 1.24	0.49 ± 0.04
OB13	56 040.174 559	4691.39 ± 0.76	98.0	48.6	16.31 ± 1.81	0.40 ± 0.04
OB14	56 065.179 567	4693.42 ± 0.48	216.7	30.7	10.69 ± 1.33	0.38 ± 0.05
OB15	56 067.230 624	4691.08 ± 0.76	66.1	48.6	12.17 ± 1.59	0.30 ± 0.04
OB16	56 096.058 511	4692.20 ± 0.27	126.8	14.1	10.56 ± 0.63	0.70 ± 0.05
OB17	56 099.028 092	4691.02 ± 0.41	50.3	26.2	10.33 ± 0.80	0.60 ± 0.05
OB18	56 101.070 920	4692.48 ± 0.35	143.1	22.4	11.55 ± 0.83	0.60 ± 0.05
OB19	56 127.003 432	4693.90 ± 0.61	228.4	39.0	11.90 ± 1.65	0.32 ± 0.05

The result of the Gaussian fit for the broad component of the He II line. The OB number, the wavelength, the FWHM and the flux is presented. The flux is in units of 10^{-17} erg cm^{-2} s^{-1} Å^{-1}. OBc, OBe, OBf and OBg are adapted from table 1 in Cseh et al. (2011). MJD values are corresponding to the middle of each OB. The barycentric corrected velocity shift (v_s) with respect to the reference point. The error on the velocity shift ($v_{s,err}$) corresponds to the wavelength uncertainty in Column 3.

was -105.71° ($N = 0^\circ$, $E = 90^\circ$). The trace for the ULX counterpart was centred on the He II λ4686 emission line profile. For the He II line profile analysis, we used a trace width of 4 pixels corresponding to 1.0 arcsec in order to isolate the ULX emission from the nebular emission. The HgCdHeNeAr lamp and standard stars provided by European Southern Observatory were used for wavelength and flux calibration. An atmospheric extinction correction was applied using the IRAF built-in Cerro Tololo Inter-American Observatory extinction tables. We corrected for the reddening using $E(B-V) = 0.08 \pm 0.03$ (Kaaret & Corbel 2009; Cseh et al. 2011) and the extinction curve from Cardelli, Clayton & Mathis (1989) with $R_V = 3.1$.

3 ANALYSIS AND RESULTS

Following Cseh et al. (2011), in each OB we fitted the He II line with a two-component Gaussian profile. First, we fitted the continuum with a second-order polynomial around each line, excluding the line itself by visual examination. The flux errors were estimated by the root-mean-square deviation of the data in the same region. For the two-component Gaussian fit we used a non-linear least-squares fit by employing the `LMFIT` subroutine, that is based on 'MRQMIN' (Press et al. 1992), of the Interactive Data Language (IDL) version 7.0.

We obtained a good fit in all but five OBs; we summarize our results in Table 2 and show OB6 as an example in Fig. 1. As noted by Cseh et al. (2011), in the 2008 data we did not detect a broad component in OBa, OBb and OBd. Similarly, in our current data set, OB1, OB3, OB7, OB20 and OB21 do not show any broad component, which is probably due to variations in its flux (see later in Section 4).

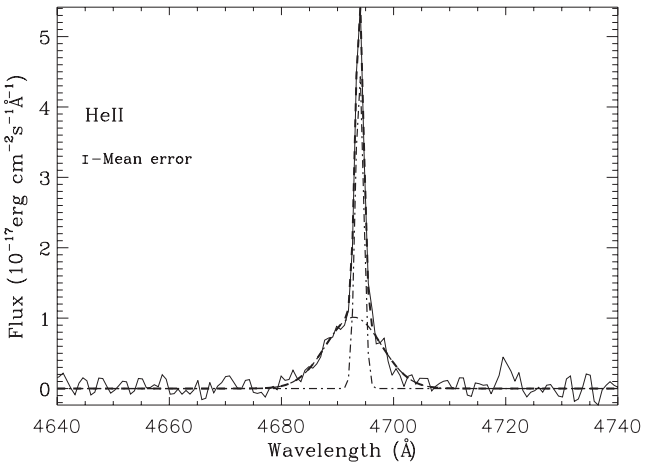

Figure 1. The figure shows the two-component Gaussian fit of the He II line of OB6 as a demonstration. The separate components are shown with dash–dotted lines, the overall fit is shown as a dashed line.

3.1 The broad component

The average full width at half-maximum (FWHM) of the broad component is $W_b = 12.2 \pm 1.0$ Å with a standard deviation of 1.6 Å. Given that the standard deviation is greater than the error on W_b, we estimate the width variation to be ∼13 per cent. The line profiles are Gaussian and the corresponding average

Table 3. Correlation tests.

Test	Kendall's τ	Probability
λ versus FWHM	0.085	0.62
λ versus Flux	0.29	0.086
FWHM versus Flux	−0.072	0.67

Correlation tests between the fitted parameters of the broad component of the He II line.

FWHM in velocity units is $v = 780 \pm 64\,\mathrm{km\,s^{-1}}$. The rms wavelength shift of the broad component of 2.89 ± 0.65 Å, corresponding to $185 \pm 42\,\mathrm{km\,s^{-1}}$, is a substantial fraction of the line width.[2]

To place a conservative upper limit on the semi-amplitude of the radial velocity excursion, we quote half of the difference between the maximum and minimum wavelength shift of the broad component (excluding OBs from 2008 that have high uncertainties due to a different spectral resolution). We find an upper limit on the semi-amplitude of $132 \pm 42\,\mathrm{km\,s^{-1}}$.

As a next step, we tested whether the wavelength shift of the broad component can be due to motion within the accretion disc, e.g. an outflowing material may cause a blue shift and a narrower line width and vice versa. To this purpose, we performed correlation tests, between the wavelength (λ) and the FWHM of the broad component, between the flux of the broad component and λ, and between the flux and the FWHM. We find no correlation in any of these parameters (Table 3).

3.2 Period search

As a next step, we performed a period search using three different methods: first, we used an epoch folding method, then a phase dispersion minimization (PDM), and finally a Lomb–Scargle (LS) periodogram analysis.

For the epoch folding period search, first, we obtained helio- and barycentric velocity corrections using an IDL implemented code called `baryvel` that is accurate to velocities of $\sim$1 m s^{-1} and based on the algorithm of Stumpff (1980). Given that the zero-point of the velocity curve is unknown, we set a reference frame to the bluest shift of the broad component; see Table 2. This results in a velocity curve that is shifted by a constant value which we fit with an additional free parameter (v_0). We note that setting the reference frame to the narrow component of the He II line may introduce bias on the shift of the broad component. This is because a nebular component can have a complex velocity structure as well as variations of $\sim$50–80 km s^{-1} (Lehmann et al. 2005).

Recent X-ray studies of NGC 5408 X-1 reveal a quasi-periodic dipping behaviour of $\sim 250 \pm 28$ d (Grisé et al. 2013; Pasham & Strohmayer 2013). Motivated by these results, we folded over a period range from 1 up to 300 d with a resolution of 10^{-4} d to match the uncertainty on the epoch of the observations. Using `LMFIT`, described above, each of these folded velocity curves were then fitted with a sinusoidal function: $v_r(\Phi) = K\cos(\Phi - \Phi_0) + v_0$, where K is the amplitude in units of km s^{-1}, Φ is the phase, Φ_0 is the phase shift in units of radian, v_0 is a constant in units of km s^{-1}. We calculated the phase for each epoch as $\Phi = 2\pi(1 - \frac{t \bmod P}{P})$, where

[2] We note that the co-added spectrum (Fig. 6) shows an apparent broad component of the Hβ line confirming previous results of Cseh et al. (2011), however, most of the OBs are not suitable for similar analysis due to a relatively low flux in the broad component.

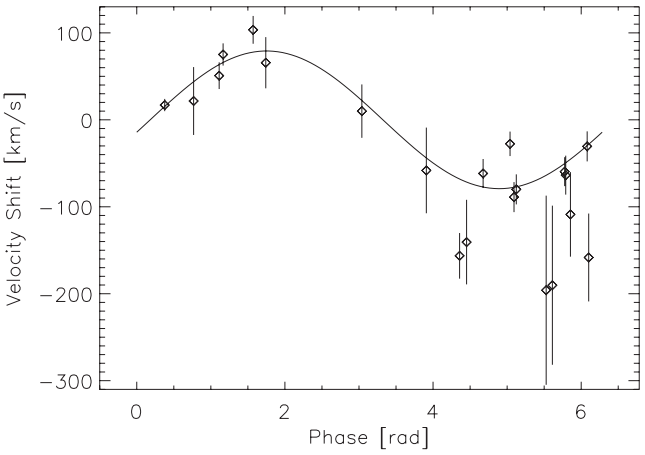

Figure 2. The figure shows an example fit of the velocity curve folded on the best fit test period.

t is the MJD date and P is the test period. We find a best-fitting test period of $P = 2.6464$ d for a χ^2/d.o.f $= 2.8$ with a semi-amplitude of the velocity curve of $K = 83 \pm 6\,\mathrm{km\,s^{-1}}$, $v_0 = 212 \pm 6\,\mathrm{km\,s^{-1}}$ and $\Phi_0 = 1.55 \pm 0.11$ in units of radian, see Fig. 2.

In order to assess the quality of the fit, we evaluated the corresponding reduced χ^2 values of each trial period (see Fig. 3). Using the same fitting method as above, we also evaluated the χ^2 value of a constant and a linear fit for a comparison. The constant fit resulted in a reduced χ^2 of 13.5 that is independent of the period range. On the other hand, for the linear fit we used a period range identical to the range of the sinusoidal fit, and minimizing the obtained χ^2 values resulted in χ^2/d.o.f. $= 2.9$. A comparison to the minimum χ^2 of the sinusoidal fit shows that there is no real period found (see below as well).

We also searched for non-sinusoidal periods using a string length method (Dworetsky 1983), which is a binless PDM (Stellingwerf 1978) suitable for sparse, unevenly sampled measurements. We folded our velocity curves and calculated phases as described above. Then, we evaluated the sum of the squared differences of the folded, phase ordered, velocity curves corresponding to each test period. On the other hand, we also estimated the significance for a period range of 1 to 150 d using 10^4 white noise simulations. We computed

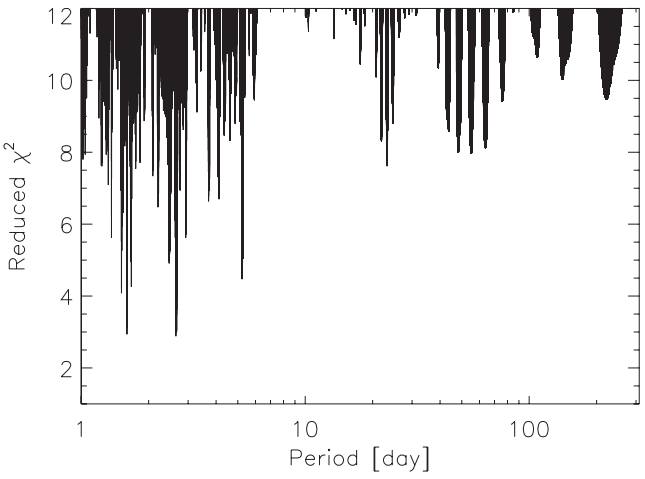

Figure 3. The figure shows the reduced χ^2 values of the sinusoidal fit as a function of period. For clarity, χ^2 values below 12 are plotted.

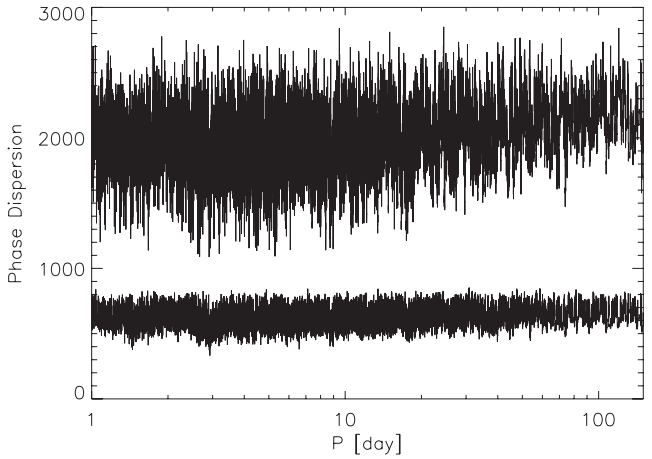

Figure 4. Phase dispersion diagram of the velocity shift of the broad component in NGC 5408 X-1. The bottom values are corresponding to a 90 per cent significance.

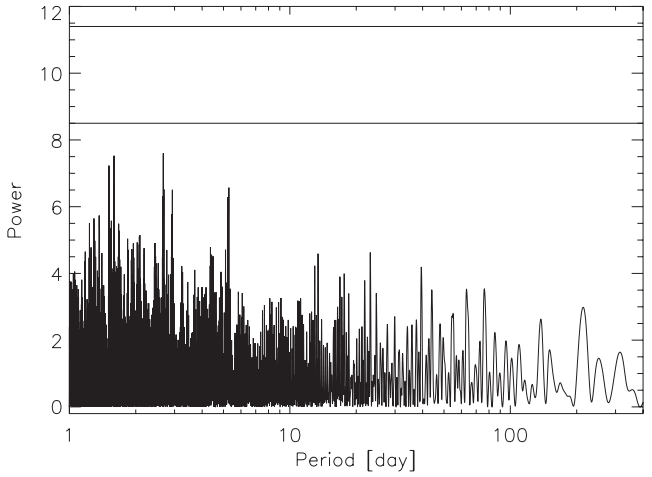

Figure 5. LS periodogram of the velocity shift of the broad component in NGC 5408 X-1. The horizontal lines correspond to 99 and 90 per cent significance, respectively.

90 per cent probabilities for each period step of 10^{-4} d separately and found no statistically significant period (Fig. 4).

Finally, we performed LS periodogram analysis (Scargle 1982) using the `scargle`[3] IDL subroutine. We estimated the significance of the periods using white noise simulations and found that there is no period above a 90 per cent probability (Fig. 5).

In summary, the data do not show any statistically significant period, regardless of the methods we use, either due to the sparse sampling or due to other effects (see Section 4.).

3.3 Donor star?

In the following, we describe our search for absorption lines that could be a signature of the donor star. To increase our signal-to-noise ratio in the optical spectrum, we averaged together all the OBs from 2010 to 2012, see Fig. 6. We note that we did not include OBs from 2008 due to a different spectral resolution.

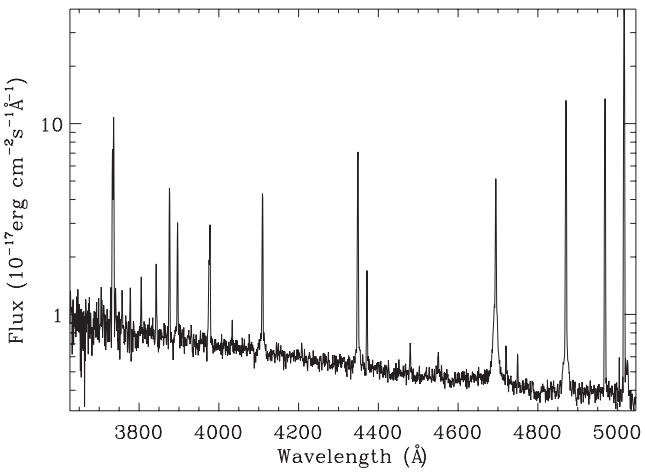

Figure 6. The figure shows the co-added spectrum of ULX NGC 5408 X-1 on a log scale. No redshift correction was applied.

Table 4. Optical lines from NGC 5408 X-1.

Name	Wavelength (Å)	Flux	FWHM (Å)
[Ar IV] 4740	4750.0	4.3 ± 0.3	1.6 ± 0.2
		9.7 ± 0.3	1.7 ± 0.2
He I 4711	4720.8	5.3 ± 0.5	2.1 ± 0.2
		12 ± 1	1.9 ± 0.2
He II 4541	4550.8	5.0 ± 0.7	3.0 ± 0.4
		9.0 ± 0.5	3.0 ± 0.3
He I 4471	4480.7	5.9 ± 0.4	2.2 ± 0.2
		19 ± 1	2.0 ± 0.1
He I 4026	4034.5	4.3 ± 0.4	1.3 ± 0.2
		8.5 ± 0.5	1.4 ± 0.1

Emission lines identified in addition to table 2 in Kaaret & Corbel (2009). The flux is in units of 10^{-18} erg cm^{-2} s^{-1}. The values in the second lines correspond to a wider trace of 16 pixel.

First, we searched for possible nebular lines (Acker et al. 1989) and identified previously unknown emission lines. We identified further transitions of He I and He II and also an argon line, see Table 4. To further test the nature of the emission lines, we also averaged the OBs using a wider trace of 16 pixels – i.e. allowing more flux from the nebula – to compare the flux of the lines to the data with the narrow trace. We find that the flux of the emission lines are increased and do not show any width variation (see Table 4), therefore the newly identified emission lines likely originate from the nebula.

Then, we made a systematic search on stellar lines using an online catalogue.[4] In particular, we looked for all highly ionized metallic absorption lines like Si, O, C, Mg that are typical for a B star. We find no absorption features in our optical spectrum. We find a typical rms level of 2.6×10^{-19} erg cm^{-2} s^{-1} Å^{-1} increasing to 3.8×10^{-19} erg cm^{-2} s^{-1} Å^{-1} in a range of 5000–4000 Å.

4 DISCUSSION

In the following section, we attempt to characterize and constrain some of the physical parameters of the binary system. First, we only

[3] http://astro.uni-tuebingen.de/software/idl/aitlib/timing/scargle.html

[4] http://cdsarc.u-strasbg.fr/viz-bin/nph-Cat/html?VI%2F26%2F

use the information on the width of the broad component, then we discuss the radial velocity curve, and finally consider the effects of disc irradiation.

We recall that the average FWHM of the broad component is $W_b = 12.2 \pm 1.0$ Å with a width variation of ∼13 per cent. This is much less than in the case of NGC 1313 X-2 that shows FWHM variation between 3 and 10 Å (Grisé et al. 2009; Roberts et al. 2011). Also, the line width in NGC 5408 X-1 remains relatively stable during the different epochs of observations, that span four years. The average FWHM of $v = 780 \pm 64\,\mathrm{km\,s^{-1}}$ is consistent with production in an accretion disc. Furthermore, the small variability may indicate a relatively stable line-emitting region. Assuming that the gas has a Keplerian motion around the black hole and the disc fills ∼70 per cent of the Roche lobe radius, we can set limits on the system parameters using equation 4 of Groot et al. (2001b) that we parametrized for NGC 5408 X-1:

$$M_{\rm BH} = 1.89 \times 10^{-8} \left(\frac{v}{\mathrm{km\,s^{-1}}}\right)^3 \left(\frac{P}{\mathrm{d}}\right) \sin^{-3} \mathrm{i}\ \mathrm{M}_\odot. \quad (1)$$

Given that the X-ray light curve of NGC 5408 X-1 shows quasi-periodic dipping behaviour, which is reminiscent to those of the high-inclination LMXBs (Grisé et al. 2013), the accretion disc is probably not face-on. In order to set a lower limit on the mass of the black hole ($M_{\rm BH}$), we assume an edge-on system ($i = 90°$). This results in $M_{\rm BH,min} = 9\left(\frac{P}{\mathrm{d}}\right)\mathrm{M}_\odot$. On the other hand, taking a minimum inclination of ∼20°, would result in $M_{\rm BH} = 224\left(\frac{P}{\mathrm{d}}\right)\mathrm{M}_\odot$. Using these constraints on $M_{\rm BH}$, the minimum orbital period of the binary system would be in the range of 19 min to 8 h. Small periods, in the order of hours,[5] are not ruled out by current observations as significant wavelength shifts are detected between consecutive observations obtained within 24 h. On the other hand, based on the hydrogen rich optical spectrum, periods below an hour are likely to be ruled out even if the smallest main-sequence donor is considered (e.g. Verbunt & van den Heuvel 1995).

Furthermore, one can estimate the inner radius of the line-emitting region (R), that corresponds to a Keplerian motion of the gas as assumed above (Groot et al. 2001b; Porter 2010); we find that $R = 2.18 \times 10^{11} \sin^2 i (\frac{M_{\rm BH}}{10\ \mathrm{M}_\odot})$ cm, which we utilize in the following sections.

4.1 Radial velocity curve

Given that no orbital period was found, we set a conservative upper limit on the semi-amplitude of the radial velocity of $K = 132 \pm 42\,\mathrm{km\,s^{-1}}$ (Section 3.1). It was empirically found that if K is inferred from disc emission line shift, then it may also be smaller by a factor of up to 2.5 than the true value (Cantrell & Bailyn 2007; Liu et al. 2012). Additionally, Grisé et al. (2013) argue that a precessing tilted disc or a warped accretion disc could also be responsible for the dipping behaviour and the highly variable X-ray count rate during these dipping periods. So, the wavelength shift could be biased by variable accretion rate and by partial illumination of the disc that could contribute to the apparent centroid shifts. Moreover, it was shown for some well-studied binary systems, that the outer part of the disc could be heavily affected or even dominated by the hotspot region, leading to distorted or non-sinusoidal radial velocity curves (Groot et al. 2001a).

[5] To evaluate the validity of a ∼19 min period, we repeated our analysis on each 15-min long individual exposure of OB8. OB8 was selected because it is moderately affected by cosmic rays around the He II line and it has a high signal-to-noise ratio of the broad component allowing us to fit these individual exposures. We find no evidence of wavelength shift (or FWHM change) between these individual exposures.

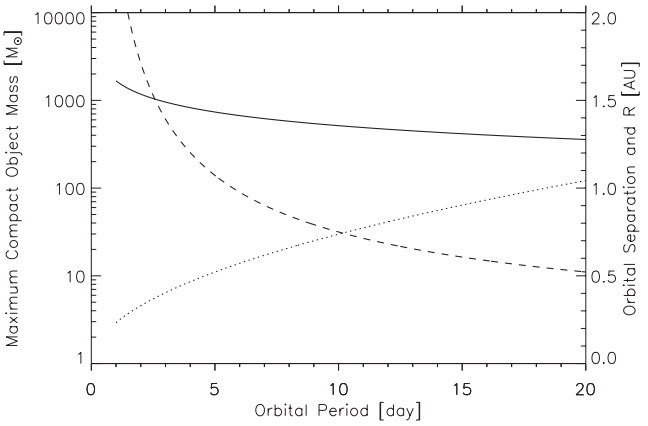

Figure 7. The figure shows the binary parameters as a function of orbital period for a specific set input of parameters (see the text). The solid line shows the mass of the black hole (left-hand scale). The orbital separation is shown as dotted line and the dashed line shows the size of the line-emitting region (both with values on the right-hand scale).

On the other hand, the rms wavelength shift of the broad component of $185 \pm 42\,\mathrm{km\,s^{-1}}$ is a substantial fraction of the line width. The line width is relatively stable and there is no correlation between e.g. the width and the shift of the broad component of the He II line (see Section 3.2). Assuming that the shift is a fraction of the true radial velocity excursion, one can characterize the mass of the black hole as a function of period. We combine the mass function and the argument that the radius of the line-emitting region (R) is smaller than the orbital separation (a). First, we obtain the mass of the black hole as a function of period using equation 2 of Cseh et al. (2011):

$$M_{\rm BH} = (M_{\rm c} \sin i)^{\frac{3}{2}} \left(\frac{PK^3}{2\pi G}\right)^{-1/2} - M_{\rm c} \quad (2)$$

where $M_{\rm c}$ is the mass of the companion, G is the gravitational constant. To obtain an upper limit one has to assume a maximum companion mass, an edge-on system (possibly consistent with the dipping behaviour), and a minimum semi-amplitude. A typical companion mass of $M_{\rm c} = 20\ \mathrm{M}_\odot$ is suggested by the extensive stellar environment studies of ULXs, including NGC 5408 X-1 (Grisé et al. 2008, 2011, 2012). Albeit a minimum semi-amplitude on the radial velocity curve is not known, we set its value to $K = 30\,\mathrm{km\,s^{-1}}$, which is a factor of ∼5 lower than our conservative upper limit and is in the range of the usually considered minimum values (see simulations by Liu et al. 2012). As a next step, one can calculate the radius of the line-emitting region as a function of period using the obtained black hole mass from equation (2). Similarly, one can evaluate the orbital separation as function of period taking into account $M_{\rm c}$. The argument of $a > R$ limits the period and consequently the mass of the black hole (Fig. 7). For these bounds, we obtain a mass of the black hole of less than $\sim 510\,\mathrm{M}_\odot$.

4.2 Disc irradiation and disc size

Disc irradiation or super-Eddington accretion can modify the disc geometry and opacity, thus the amount and the radius where the X-ray (or total) luminosity is thermalized. However, these

models might be mutually exclusive because, in the case of super-Eddington accretion, the soft X-rays are interpreted as due to a wind/outflow, that would not show reprocessed optical emission (Poutanen, Zdziarski & Ibragimov 2008; Kaaret & Corbel 2009). Additionally, super-Eddington sources may show beamed emission (Middleton et al. 2013).

This is in contrast to NGC 5408 X-1, that does not show significant beaming (Kaaret & Corbel 2009). Its SED can be well fitted with a disc irradiation model, resulting in an outer disc radius of $R_{\rm out} = (1–5) \times 10^{12}$ cm for a face-on disc (Grisé et al. 2012). Also, we recall that the X-ray count rate drops by a factor of 35 or more below average on a quasi-periodic basis (Grisé et al. 2013). In addition, the broad component of the He II line was not visible during several observations, spread across years (in 2008 OBa, OBb, OBd, in 2011 OB1, OB3, OB7, in 2012 OB20 and OB21). Except OB7, all of these observations were obtained outside the X-ray coverage. OB7 falls into a time range where dips might be expected (see figs 1 and 3 in Grisé et al. 2013). Considering the large width of the broad component as well, the optical emission is likely due to disc irradiation.

So, assuming that disc irradiation is the main contributor to the optical emission, one may compare the outer disc radius ($R_{\rm out}$) to the inner radius of the line-emitting region (R, see before Section 4.1.) to constrain the mass of the black hole. Copperwheat et al. (2007) argue that the relative contribution of disc irradiation with respect to irradiation by a donor star scales as $\cos i$, i.e. no contribution from the disc for an edge-on system and vice versa. To have a dominant disc contribution one has to consider $\cos i > 0.5$, i.e. $i < 60^\circ$. Comparing the radii, R and $R_{\rm out}$, and taking into account that $R_{\rm out} \propto \cos^{-0.5} i$, we find a black hole mass of $\sim$431–1985 $M_\odot$ for $60^\circ > i > 20^\circ$. On the other hand, it is uncertain whether the region where the He II line genesis takes place extends to the outer disc radius derived from the disc irradiation model. Therefore, this mass estimate should be taken as an upper limit.

5 CONCLUSION

We studied the optical spectrum of the ULX NGC 5408 X-1 using multi-epoch VLT observations in 2011 and in 2012. We attempted to measure the radial velocity curve using the broad component of the He II emission line, that is consistent with an origin in the accretion disc. The data do not show any statistically significant periodicity and we obtained an upper limit on the semi-amplitude of the putative radial velocity curve of $K = 132 \pm 42\,{\rm km\,s^{-1}}$. Thanks to the number of observations obtained, we identified previously unknown nebular lines; and we found no absorption lines that could be indicative of a donor star.

We also showed that the width of the broad component is relatively stable and its flux is variable, which we interpret as an effect of disc irradiation. A disc irradiation model would imply a black hole mass smaller than $\sim$431–1985 $M_\odot$, depending on inclination. Using a different approach and a conservative set of binary parameters, we find that the mass of the black hole is less than $\sim$510 $M_\odot$. Our results do not rule out the presence of a stellar-mass black hole, and suggest that future optical observations should probe an unexplored period range from a couple of hours to a few days.

ACKNOWLEDGEMENTS

Based on observations made with ESO Telescopes at the La Silla or Paranal Observatories under programme ID 087.D-0156(A) and 089.D-0646(A).

REFERENCES

Acker A., Jasniewicz G., Koeppen J., Stenholm B., 1989, A&AS, 80, 201
Cantrell A. G., Bailyn C. D., 2007, ApJ, 670, 727
Cardelli J. A., Clayton G. C., Mathis J. S., 1989, ApJ, 345, 245
Copperwheat C., Cropper M., Soria R., Wu K., 2007, MNRAS, 376, 1407
Cseh D., Grisé F., Corbel S., Kaaret P., 2011, ApJ, 728, L5
Cseh D. et al., 2012, ApJ, 749, 17
Dworetsky M. M., 1983, MNRAS, 203, 917
Farrell S. A., Webb N. A., Barret D., Godet O., Rodrigues J. M., 2009, Nat, 460, 73
Feng H., Soria R., 2011, New Astron. Rev., 55, 166
Foster D. L., Charles P. A., Holley-Bockelmann K., 2010, ApJ, 725, 2480
Foster D. L., Charles P. A., Swartz D. A., Misra R., Stassun K. G., 2013, MNRAS, 432, 1375
Gladstone J. C., Copperwheat C., Heinke C. O., Roberts T. P., Cartwright T. F., Levan A. J., Goad M. R., 2013, ApJS, 206, 14
Grisé F., Pakull M. W., Soria R., Motch C., Smith I. A., Ryder S. D., Böttcher M., 2008, A&A, 486, 151
Grisé F., Pakull M. W., Soria R., Motch C., 2009, in Rodriguez J., Ferrando P., eds, AIP Conf. Ser. Vol. 1126, The ULX NGC 1313 X-2: an Optical Study Revealing an Interesting Behavior. Am. Inst. Phys., New York, p. 201
Grisé F., Kaaret P., Pakull M. W., Motch C., 2011, ApJ, 734, 23
Grisé F., Kaaret P., Corbel S., Feng H., Cseh D., Tao L., 2012, ApJ, 745, 123
Grisé F., Kaaret P., Corbel S., Cseh D., Feng H., 2013, MNRAS, 433, 1023
Groot P. J., Rutten R. G. M., van Paradijs J., 2001a, A&A, 368, 183
Groot P. J., Nelemans G., Steeghs D., Marsh T. R., 2001b, ApJ, 558, L123
Hutchings J. B., Crampton D., Cowley A. P., Bianchi L., Thompson I. B., 1987, AJ, 94, 340
Kaaret P., Corbel S., 2009, ApJ, 697, 950
Kaaret P., Corbel S., Prestwich A. H., Zezas A., 2003, Sci, 299, 365
Kaaret P., Simet M. G., Lang C. C., 2006, ApJ, 646, 174
Lang C. C., Kaaret P., Corbel S., Mercer A., 2007, ApJ, 666, 79
Lehmann I. et al., 2005, A&A, 431, 847
Liu J., 2009, ApJ, 704, 1628
Liu J., Orosz J., Bregman J. N., 2012, ApJ, 745, 89
Middleton M. J. et al., 2013, Nat, 493, 187
Motch C., Pakull M. W., Grisé F., Soria R., 2011, Astron. Nachr., 332, 367
Pasham D. R., Strohmayer T. E., 2013, ApJ, 764, 93
Porter R. L., 2010, MNRAS, 407, L59
Poutanen J., Zdziarski A. A., Ibragimov A., 2008, MNRAS, 389, 1427
Press W. H., Teukolsky S. A., Vetterling W. T., Flannery B. P., 1992, Numerical Recipes in C. The Art of Scientific Computing, 2nd edn. Cambridge Univ. Press, Cambridge
Roberts T. P., Gladstone J. C., Goulding A. D., Swinbank A. M., Ward M. J., Goad M. R., Levan A. J., 2011, Astron. Nachr., 332, 398
Scargle J. D., 1982, ApJ, 263, 835
Soria R., Kuntz K. D., Winkler P. F., Blair W. P., Long K. S., Plucinsky P. P., Whitmore B. C., 2012, ApJ, 750, 152
Stellingwerf R. F., 1978, ApJ, 224, 953
Strohmayer T. E., 2009, ApJ, 706, L210
Stumpff P., 1980, A&AS, 41, 1
Sutton A. D., Roberts T. P., Walton D. J., Gladstone J. C., Scott A. E., 2012, MNRAS, 423, 1154
Tao L., Feng H., Grisé F., Kaaret P., 2011, ApJ, 737, 81
Tody D., 1993, in Hanisch R. J., Brissenden R. J. V., Barnes J., eds, ASP Conf. Ser. Vol. 52, IRAF in the Nineties. Astron. Soc. Pac., San Francisco, p. 173
Verbunt F., van den Heuvel E. P. J., 1995, X-ray Binaries. Cambridge Univ. Press, Cambridge, p. 457
Walton D. J., Roberts T. P., Mateos S., Heard V., 2011, MNRAS, 416, 1844
Webb N. et al., 2012, Sci, 337, 554
Zampieri L., Impiombato D., Falomo R., Grisé F., Soria R., 2012, MNRAS, 419, 1331

This paper has been typeset from a TEX/LATEX file prepared by the author.